Nanotechnology

ACCEPTED MANUSCRIPT

Zn- and (Mn, Zn)-substituted versus unsubstituted magnetite nanoparticles: Structural, magnetic and hyperthermic properties

To cite this article before publication: Nataša Jovi Orsini *et al* 2020 *Nanotechnology* in press https://doi.org/10.1088/1361-6528/ab76e7

Manuscript version: Accepted Manuscript

Accepted Manuscript is “the version of the article accepted for publication including all changes made as a result of the peer review process, and which may also include the addition to the article by IOP Publishing of a header, an article ID, a cover sheet and/or an ‘Accepted Manuscript’ watermark, but excluding any other editing, typesetting or other changes made by IOP Publishing and/or its licensors”

This Accepted Manuscript is **© 2020 IOP Publishing Ltd**.

During the embargo period (the 12 month period from the publication of the Version of Record of this article), the Accepted Manuscript is fully protected by copyright and cannot be reused or reposted elsewhere.
As the Version of Record of this article is going to be / has been published on a subscription basis, this Accepted Manuscript is available for reuse under a CC BY-NC-ND 3.0 licence after the 12 month embargo period.

After the embargo period, everyone is permitted to use copy and redistribute this article for non-commercial purposes only, provided that they adhere to all the terms of the licence https://creativecommons.org/licences/by-nc-nd/3.0

Although reasonable endeavours have been taken to obtain all necessary permissions from third parties to include their copyrighted content within this article, their full citation and copyright line may not be present in this Accepted Manuscript version. Before using any content from this article, please refer to the Version of Record on IOPscience once published for full citation and copyright details, as permissions will likely be required. All third party content is fully copyright protected, unless specifically stated otherwise in the figure caption in the Version of Record.

View the article online for updates and enhancements.

This content was downloaded from IP address 168.96.255.100 on 20/02/2020 at 16:23

Zn- and (Mn, Zn)-substituted *versus* unsubstituted magnetite nanoparticles: Structural, magnetic and hyperthermic properties

N. JoviĹ Orsini[1*], M. M. MiliĹ[1] and T. E. Torres[2]

[1]Institute of Nuclear Sciences òVinļaò, Laboratory of Theoretical Physics and Condensed Matter Physics (020), University of Belgrade, P.O. Box 522, RS-11001 Belgrade, Serbia

[2]Instituto de Nanociencia de Aragón and Departamento de Fisica de la Materia Condensada, Universidad de Zaragoza, Mariano Esquillor s/n 500018, Zaragoza, Spain

[*]Corresponding Author:

Dr. Nataġa JoviĹ Orsini

ORCID iD: https://orcid.org/0000-0003-1613-3361

E-mail:natasaj@vin.bg.ac.rs

Abstract

In this work, we studied structural and magnetic properties of 18nm-sized Zn-substituted magnetite, 28nm-sized unsubstituted and 17nm-sized (Mn,Zn)-substituted iron oxide nanoparticles, synthesized by thermal decomposition method. Their features were examined by analyzing the X-ray diffraction (XRD) data, ^{57}Fe Mössbauer spectra and magnetization measurements by SQUID interferometer. The microstructure was inspected comparing different the size and strain broadening models incorporated into *Fullprof* software. In terms of crystallinity and size dispersion, applied synthesis protocol shows superiority over decomposition of iron oleate and the co-precipitation synthesis route. The saturation magnetization at T=5 K was found to be within the M_S=91.2-98.6 Am^2/kg range, while at 300 K M_S of pure and Zn-substituted Fe_3O_4 nanoparticles is 83.6 and 86.2 Am^2/kg, respectively. Effective magnetic anisotropy constant K_{eff}, estimated under slow measurements by SQUID, is below 20 kJ/m^3 in all three samples. Some preliminary measurements of the magnetic hyperthermia performance, expressed via Specific Absorption Rate (*SAR*) value showed that the best heating performances were displayed by 18nm-sized oleic acid-coated $Zn_{0.13}Fe_{2.87}O_4$ cubo-octahedrons with *SAR*≅425 W/g$_{Fe}$ at H_0=20 kA/m and f=228 kHz.

Accepted Manuscript

Keywords: magnetite-based nanoparticles, Mössbauer spectroscopy, magnetic hyperthermia, microstructure

1. INTRODUCTION

Magnetite (Fe_3O_4) and a series of mixed spinel ferrites ($MO{\cdot}Fe_2O_3$, M being the divalent transition metal cations) have been of a technological and scientific interest for a long time. Their nanoparticulate forms have been exploited in medicine and new technologies in the last decades [1-4]. Due to the satisfied biocompatibility and biodegradability, ferrofluids based on superparamagnetic iron oxide-based nanoparticles (IONPs) have high potential for applications in medical diagnostic and curing procedures, particularly as contrast media for biomedical imaging (magnetic particle (MPI) or resonance (MRI) imaging) [5, 6] as magnetically-driven drug/gene delivery systems [7] or magnetic thermoseeds for magnetic particle hyperthermia (MPH) treatment of ill tissues [7-12]. Other iron oxide-based nanostructures, such as dumbbell, porous, core/shell, hollow or hybrid ones, have been also investigated for biomedical applications [13].

The applicability of the magnetic nanoparticles in biomedicine is closely related to their own characteristics such as magnetic and microstructural features (e.g. size and shape, surface chemistry, composition, degree of crystallinity). Another important item, which should be considered regarding their bio-applicability is the way how MNPs interact with cells. The magnetic properties of nanoparticles are usually altered in *in vivo* conditions due to the unavoidable nanoparticle's clustering and movement restriction after interaction with cells [14]. Consequently, their biomedical performances are changed.

One of the promising application of superparamagnetic IONPs is their use for magnetic hyperthermia therapy [7-12]. Under exposure to an alternating magnetic field, superparamagnetic IONPs suspended in a fluid can absorb energy from the applied AC magnetic field and release it as heat. If they are properly functionalized and located in ill tissues, they will be able to inhibit activity of cancer cells by locally increasing temperature [7, 12]. To improve the heating efficiency, IONPs should possess the optimal size and shape, narrow size distribution and enhanced magnetic performances (e.g. high M_S and K_{eff} value). In recent years, remarkable

Accepted Manuscript

achievements in tailoring the optimal size and shape of nanoparticles have been accomplished [9, 10, 15, 16]. Once that the particle size close to the critical value (related to the transition from superparamagnetic to ferrimagnetic regime) is reached, further increase of the heating efficiency can be achieved by changing the composition of IONPs from pure (Fe_3O_4) toward substituted-magnetite ($Fe_{3-x}M_xO_4$) nanoparticles [1, 5, 17]. It was shown that Zn-substituted Fe_3O_4 nanoparticles represent one of the best choices, due to the low toxicity of Zn ions and the positive impact of Zn-ion substitution on the magnetic saturation value. Magnetite is a typical inverse spinel with one half of Fe^{3+} ions in tetrahedral (A) sites, and the second half of Fe^{3+} and all Fe^{2+} ions in octahedral (B) sites. The effect of magnetic Fe^{3+} ions substitution by diamagnetic Zn^{2+} ones at the tetrahedral, A-sites of the spinel lattice (represented by the formula AB_2O_4 (S.G. $Fd\bar{3}m$)), is well known and visible by increases of the saturation magnetization, M_S, for doping level up to x≈0.4 [18]. Relating to hyperthermia or magnetic sensing potential, superiority of cubic over spherical nanoparticles has been revealed, as well as of Zn-doped over pure Fe_3O_4 nanoparticles [6, 19, 20]. Recently, it has been revealed that silica-coated nonstoichiometric Gd-Zn ferrite exhibits the most promising therapeutic capability at relatively low particle concentrations [8]. Further improvement in the heating performances has been observed when Fe_3O_4 nanoparticles change shape and move from 3-dim objects (spherical and cubic) to 1-dim objects (nanorods) [15]. In terms of interparticle interactions, *Tong* et al., reported that well dispersed 33 nm sized ferromagnetic iron oxide nanocrystals heat much better than their aggregates [9].

Along with magnetic properties, the microstructure of nanoparticles is important item in defining the nanoparticleôs biomedical performances [21-25]. For that reason, a closer relation between the degrees of the nanoparticles crystallinity, phase composition and the magnetic response should be established. It could give better insight into understanding of hyperthermia efficiency of magnetic nanoparticles.

In this paper, we report on the structural, magnetic and hyperthermic characteristics of three samples, composed of unsubstituted, Zn- and (Mn,Zn)-substituted Fe_3O_4 nanoparticles, synthesized by thermal decomposition method. We discuss the main advantages of this method (e.g. production of well crystallized nanoparticles with narrow size distribution) keeping in mind all shortcomings (use of expensive and environmentally harmful substances, need of a post-synthesis treatment to transfer nanoparticles into water, etc.). The degree of crystallinity and

Accepted Manuscript

microstrains in the samples were evaluated from refinement of the XRD data using the *Fullprof* program. Different combinations of the size and strain broadening models were tested (isotropic *vs*. anisotropic), and the comparative analysis was done. Magnetic characterization of the powdered samples was performed using the Mössbauer spectroscopy and measurements by SQUID. Some preliminary measurements of the magnetic hyperthermia performance (expressed via the *SAR* value), were carried out on ferrofluids made of oleic acid-coated Fe_3O_4 nanoparticles (pure and substituted), dispersed in hexane, under physiologically tolerable AC magnetic field conditions.

2. MATERIALS AND METHODS

2.1 Chemicals

Iron(III) acetylacetonate ($Fe(acac)_3$, ≥99.9% p.a. Sigma Aldrich), zinc(II) acetylacetonate hydrate ($Zn(acac)_2$·hydrate, Aldrich), zinc(II) chloride ($ZnCl_2$, ≥97%, Sigma Aldrich), iron(II) chloride tetrahydrate ($FeCl_2 \cdot 4H_2O$, ≥99.0% p.a. Sigma Aldrich), benzyl ether (98%, Aldrich), oleic acid (techical grade, >90%, Aldrich), oleylamine (techical grade, >70%, Aldrich).

2.2 Synthesis of magnetite-based cuboctahedral nanoparticles

Unsubstituted and Zn- and (Mn, Zn)-substituted magnetite nanoparticles were synthesized by thermal decomposition of metal precursors (acetylacetonate and chloride salts), in benzyl ether, under bubbling of nitrogen, in the presence of oleic acid and oleylamine as surfactants. Not any reducing agent was used. The concentration of metal cations was kept constant at 0.1 mol per dm^3 of solvent. The molar ratios of the used reactants, given in the table 1, were set up according to the desired compositions of the products: $Zn_{0.4}Fe_{2.6}O_4$, in samples **1** and **2**, and $Mn_{0.5}Zn_{0.5}Fe_2O_4$ in sample **3**. Due to the fact that incorporation of Zn^{2+} ions into a spinel structure is difficult to achieve when this synthesis route is chosen, two different sources of Zn^{2+} ions were used, $Zn(acac)_2$ (sample **1**) or $ZnCl_2$ salt (samples **2** and **3**). In the sample **2**, the $FeCl_2 \cdot 4H_2O$ precursor was used as a source of Fe^{2+} ions.

Accepted Manuscript

Table 1 Molar ratios of metal precursors, oleic acid (OA) and oleylamine (OM), dissolved in 60 mL of benzyl ether.

Sample	$Zn(acac)_2$·hydrate (mmol)	$Fe(acac)_3$ (mmol)	$MnCl_2 \cdot 4H_2O$ (mmol)	$ZnCl_2$ (mmol)	$FeCl_2 \cdot 4H_2O$ (mmol)	OA (mmol)	OM (mmol)	Actual stoichiometry (EDX)
1-Z18	0.8	5.2	-	-	-	24	-	$Zn_{0.13}Fe_{2.87}O_4$
2-F28	-	4	-	0.8	1.2	18	18	Fe_3O_4
3-MZ17	-	4	1	1	-	18	18	$Mn_{0.06}Zn_{0.04}Fe_{2.9}O_4$

In a typical procedure, the Zn-containing sample **1** (i.e. **Z18**) was synthesized starting from a mixture of $Zn(acac)_2$·hydrate (0.8 mmol), $Fe(acac)_3$ (5.2 mmol), oleic acid (24 mmol), and 60 mL of benzyl ether (the cations-to-OA molar ratio was kept at 1:4). The mixture was poured in a three neck flask (250 mL volume) and mechanically stirred at room temperature for 30 minutes under nitrogen flow. The heating started, first up to 200 °C, followed by aging for ~2 hours at that temperature, and then up to the boiling temperature of the mixture (~290 °C) under refluxing conditions (see figure S1). A heating rate to reflux was around 8 °C/min, and the reaction time was about one hour. Afterwards, the flask was removed from a heating mantle and the product of reaction was left to cool down to room temperature. The black precipitate was magnetically collected, washed two or three times in an excess of ethanol and hexane, and re-dispersed in hexane. Similarly, the synthesis of samples **2** and **3** were carried out starting from the mixture of reactants listed in table 1. But, for preparation of these two samples $ZnCl_2$ salt was used as a precursor of Zn^{2+} ions and, in addition to oleic acid, oleylamine was used, too (the cations-to-OA-to-OM molar ratio was 1:3:3). The heating rates ($\partial T/\partial t$), the aging time, t_{aging} (2 hours at the ramp and 1 hour under refluxing), and the reaction temperatures (T_r ~ 290-270 °C) were kept almost the same in all three synthesis.

2.3 Characterization

Morphology, structure, microstructure and composition of the samples were analyzed by Transmission Electron Microscopy (TEM), X-ray diffraction (XRD) and Energy-Dispersion X-ray (EDX) spectroscopy. Magnetic properties were studied from ^{57}Fe Mössbauer spectra analysis and the temperature and field dependence of magnetization (measured by SQUID). The

Accepted Manuscript

powdered specimens of the prepared samples, used for characterization, were obtained after precipitation of nanocrystals from hexane upon adding ethanol and drying under nitrogen flow.

TEM (FEI TECNAI T20, 200 kV) and HRTEM (FEI TECNAI T30, 300 kV) microscopes were used to examine the nanoparticles morphology, average size and size distribution. Nanoparticle specimens for TEM were prepared by placing a drop of a diluted solution (in hexane) onto a carbon-coated cupper grid. Images were analyzed using the *DigitalMicrograph* program. To estimate the average particle size from TEM, between 200 and 400 nanoparticles were counted. Electron microprobe analyses were obtained using a scanning electron microscope (SEM) connected with an energy-dispersion X-ray analysis (EDX) unit.

XRD patterns of all three samples were collected using *Rigaku SmartLab* diffractometer and Cu $K\alpha$ and $K\beta$ radiation. The XRD data were collected in a 2θ range between 10 and 90 or 100°, with the step-size of 0.02°, and a speed counting rate of 0.2°/s. The collected data were fitted using the program *Fullprof* based on the Rietveld method. Both, structural and microstructural parameters were refined for all samples in the space group $Fd\bar{3}m$ (No.227), assuming a spinel structure. XRD peak profiles were modeled by the Thomson-Cox-Hasting modified pseudo-Voigt (TCH-pV) function. A correction for instrumental broadening was done considering the experimental profile as a convolution of the instrumental profile and the specimen profile. The instrumental resolution function (IRF) was obtained upon refinement of the standard, lanthanum hexaboride (LaB_6). Following structural parameters: lattice constant, a, fractional coordinates for oxygen in 32e site and isotropic displacement parameters, B, as well as microstructural parameters: the average crystallite size, d_{XRD}, and microstrain, were fitted. The background was refined using linear interpolation between selected points.

Magnetic properties of the samples were studied using the Mössbauer spectroscopy and measurements of the magnetization by MPMS XL-5 SQUID magnetometer. The Mössbauer spectra of samples were collected at room temperature, in transmission geometry using a ^{57}Co γ-ray source within a Rh matrix. The velocity scale was calibrated relative to standard α-Fe foil. The best fit of the spectra was achieved considering a distribution of magnetic sextets through Voigt-based profile analysis (χ^2 close to one). Field-cooled (FC) and zero-field-cooled (ZFC) DC magnetization measurements were performed in a magnetic field of 7.96 kA/m (100 Oe), in the 5-300 K temperature range, following standard protocol. Hysteresis loops, M(H), were recorded at 5 and 300 K at magnetic field up to 3978.88 kA/m (50 kOe). To calculate the mass

Accepted Manuscript

magnetization accurately, the thermogravimetric analysis (TGA) and the differential thermal analysis (DTA) were employed using a TA SDT 2960 instrument. TGA/DTA analysis was performed in air, at a heating rate of 10 °C/min, up to 700 °C. The weight loss due to evaporation of organic phase (in wt%), obtained by the TGA/DTA analysis, was re-calculated taking into account that during heating the partial oxidation takes place, bringing in a mixture of hematite and magnetite phases (proved by the XRD analysis of thermally treated samples; not shown).

Preliminary measurements of the heating efficiency of here investigated ferrofluids composed of iron oxide-based nanoparticles (**1**, **2**, and **3**) dispersed in hexane, were done using a calorimetric analyzer (DM 100 Series, by *nBnanoScale Biomagnetics*, Spain). The specific absorption rate (*SAR*) of all samples was determined from the measurement of the temperature rise in time, $T(t)$, when the ferrofluids (previously placed in a 2 ml glass holder) were exposed to an alternating magnetic field, $H = H_0 \, sin(\omega t)$ (H_0 - is the magnetic field amplitude, and ω - is an angular velocity) [7]. The $T(t)$ curves were recorded using an optical fiber temperature probe immersed inside the ferrofluids. During the measurements, a glass holder with ferrofluids **1** and **2** was placed in a high-vacuum environment allowing us to consider almost adiabatic conditions of *SAR* measurements. The $T(t)$ curves for ferrofluid **3** were recorded five months later under slightly different conditions (frequency was 252 kHz (instead of 228 kHz) and without vacuum isolation). The following expression was used to estimate *SAR* value: $SAR(W/g_{Fe}) \cong \rho_{hexane} \times c_{hexane} \times (\Delta T/\Delta t)_{max} \times [x_{Fe}]^{-1}$, where $\rho_{hexane} = 654.8$ kg/m^3 is the density and $c_{hexane} = 2.26$ J/g °C is the specific heat capacity of hexane, $(\Delta T/\Delta t)_{max}$ is the initial slope of the heating curve $T(t)$ and $[x_{Fe}]$ is the average concentration of Fe^{3+} ions in ferrofluids. The $[x_{Fe}]$ was determined comparing the UV-vis absorbance of Fe^{3+} ions from sample solutions (after oxidation) with the calibration curve obtained measuring the UV-absorbance of patron solutions of known, but different Fe^{3+} concentrations [26]. Patron solutions were prepared from iron standard solution (in a mixture of 6M H_2SO_4 and 65% HNO_3). The absorbance was measured by UV-visible spectrometer when solution was exposed to irradiation (λ = 480 nm).

2.4 Rietveld refinement

The structural and microstructural parameters of Zn-doped (sample **1**), unsubstituted (sample **2**), and (Mn,Zn)-containing (sample **3**) magnetite, were refined in a model in which the stoichiometry of the samples was adjusted according to the results obtained by EDX analysis

Accepted Manuscript

(see figure S2). The cations distribution was modeled in accordance with the preferred cations occupancy and not refined. Such an assumption is reliable since, for X-rays, ions with low electron density difference do not distinguish significantly. In the Zn- and (Mn,Zn)-containing magnetite all zinc cations occupy tetrahedrally coordinated, 8*a* sites (A-sites). Although in nanostructured Zn-doped magnetite ($Zn_xFe_{3-x}O_4$), the Zn^{2+} ions can occupy both A and B sites, for x<0.4, the Zn^{2+} ions follow their high preference for tetrahedral A-sites, valid for bulk materials [5, 18]. In addition, cations distribution in the (Mn,Zn)-doped sample was previously set up in the way so that all manganese ions were considered to be +2 valence and in A-sites, even though it is known that the manganese ions can easily vary the valence state (between +2/+3), and that Mn^{3+} ions preferably occupy octahedral, B-sites (16*d*) [27]. After refinement of the Mössbauer spectra, the presence of Mn^{3+} ions in B-sites was allowed. The attempt to refine occupation parameters of cations and to determined the cations distribution failed due to the fact that the zinc ($3d^{10}4s^2$) and iron ($3d^64s^2$) are the fourth, while manganese ($3d^54s^2$) and iron are the nearest neighbours in the periodic system. As such, they are hardly distinguished for X-rays. In addition, refinement of the crystal structure solely, when pseudo-Voigt function was used to delineate diffraction profiles and the instrumental broadening was disregarded, gave very good agreement between experimental and refined XRD patterns, regardless the cations distribution over the 8*a* and 16*d* sites.

When the microstructural analysis was applied, the XRD peak profiles were modeled by the TCH-pV function and the IRF function was included (see section 2.3). Different combinations of the isotropic/anisotropic *size* and *strain* broadening were considered during refinement. An anisotropic size broadening was considered as a linear combination of spherical harmonics (SPH) [28]. In the case of an anisotropic *strain* broadening, the Stephens parameters, S_{400} and S_{220}, for $m3m$ symmetry, were refined [28, 29].

3. RESULTS AND DISCUSSION

3.1 Composition, morphology and size

The experimental XRD patterns of all three samples, **1, 2** and **3**, are shown in the figure S3 (see *Supplementary Info*). All reflections were indexed in a spinel structure with cubic symmetry (space group *Fd*-3*m*, No. 227). The reflection at $2\theta \sim 32°$ with very low intensity (observed in all

Accepted Manuscript

three XRD patterns), is a satellite of the major (311) spinel reflection caused by Cu *K*β radiation of wavelength 1.39217 Å. It might be accidentally ascribed to the (100) reflection of ZnO phase. Since, no improvement in the crystal structure refinement was observed in a two phases model, ZnO phase presence was ruled out. The presence of hematite or FeO as an impurity was excluded in all three samples due to the results of Mössbauer spectra analysis (see forthcoming results).

The EDX analysis on selected surfaces of the studied samples showed that the amount of incorporated Zn and Mn ions into the spinel structure is notably lower than it was set up by the initial stoichiometry of precursors (table 1). According to it, the sample **1** is Zn-doped, the sample **2** is unsubstituted, while the sample **3** is (Mn,Zn)-containing magnetite, with the stoichiometry $Zn_{0.13}Fe_{2.87}O_4$, Fe_3O_4 and $Mn_{0.06}Zn_{0.04}Fe_{2.9}O_4$, respectively.

TEM images of the samples **1**, **2** and **3**, and their size distributions are shown in figure 1. The highest uniformity of particles size and shape is achieved in the sample **1**. It is evident that most of the nanoparticles are cubo-octahedra-like in shape. Nanoparticles with shapes different than those are observed in the samples **2** and **3**, but significantly less in number. Average edge dimensions of the nanoparticles, obtained by fitting the size distribution with Gauss function, were found to be 18.3, 28.1 and 17.2 nm for **1**, **2** and **3**, respectively. According to the results of EDX and TEM analysis we re-label the samples as: **1** is **Z18**, **2** is **F28** and **3** is **MZ17**, where the capital latter indicate composition, while the number indicates the average particle size.

For the sake of comparison, Zn-substituted Fe_3O_4 nanoparticles were synthesized following the classical thermal decomposition synthesis (when 1,2-hexadecanediol was used as a reducing agent). Thus obtained nanoparticles are quasi-spherical with an average diameter ~10 nm (figure S4). Based on the literature data, the polyalcohol, when acting as a reducing agent, can produce polyaldehydes and polyorganic acids, whose presence during the synthesis can suppress formation of bigger nanoparticles [30]. Thus, partial reducing or avoiding adding of polyalcohol in the synthesis seems to be the easiest way to obtain bigger nanoparticles. In addition, by fine tuning of the cations/capping ligands molar ratio and the heating rate to reflux, it is possible to further manipulate the size and shape of nanoparticles [16]. Such an approach in the thermal decomposition of metal precursors becomes competitive to the co-precipitation synthesis route [22, 23], the two steps synthesis via decomposition of iron oleate complexes [31,

Accepted Manuscript

32], or polyol method [33], in the sense of designing bigger nanoparticles with high degree of crystallinity and low density of defects.

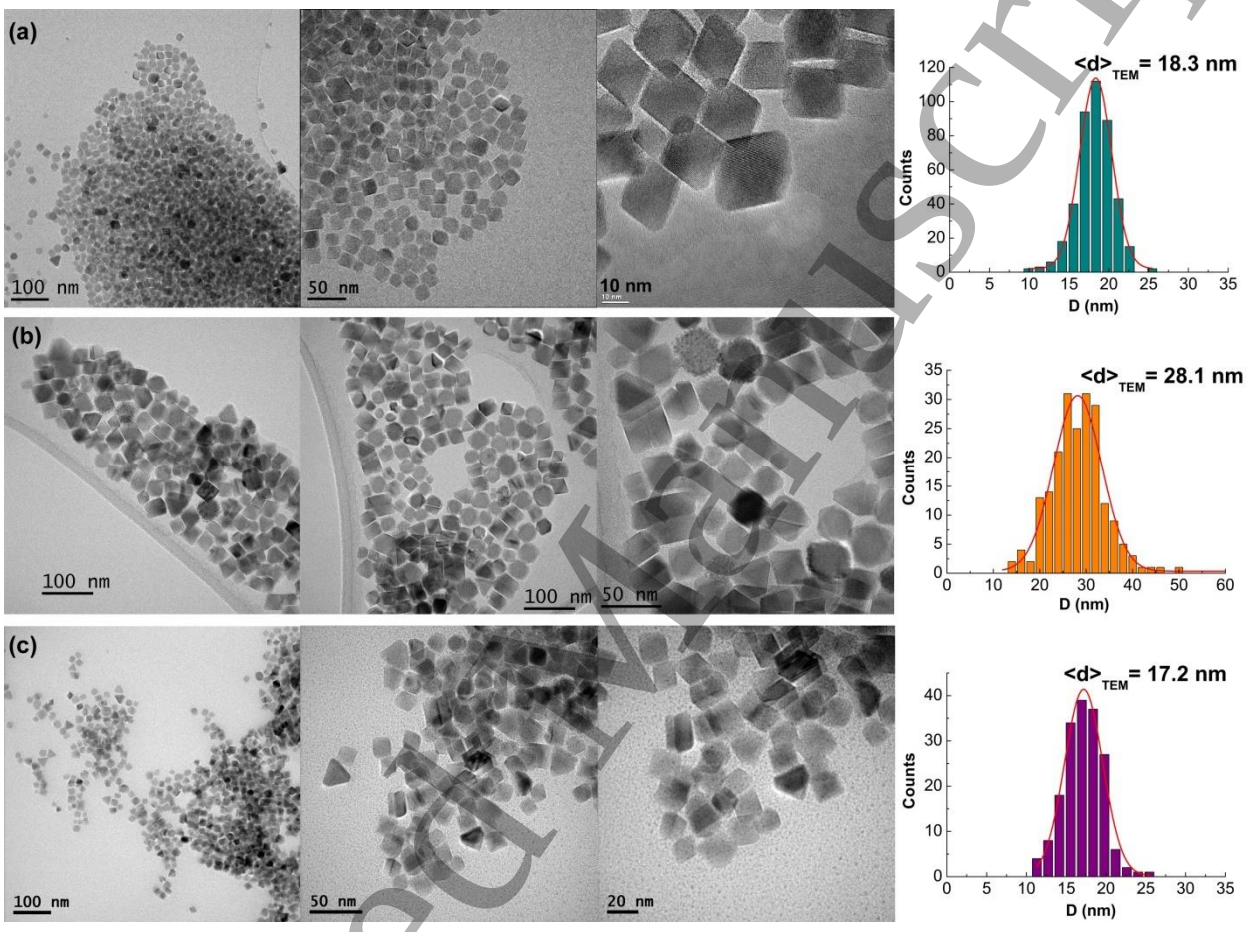

Figure 1. TEM images of the samples: (a) **1-Z18**, (b) **2-F28** and (c) **3-MZ17**, with the stoichiometry $Zn_{0.13}Fe_{2.87}O_4$, Fe_3O_4 and $Mn_{0.06}Zn_{0.04}Fe_{2.9}O_4$, respectively.

Following the above mentioned modification in the synthesis procedure, it seems that Zn^{2+} ions are built in into the spinel structure more efficiently when $Zn(acac)_2$ salt is used (sample **1**), instead of $ZnCl_2$ precursor (samples **2** and **3**). Generally, building-in Zn ions into the spinel structure is difficult and dependent on the used precursors for Zn ions [5, 17, 34, 35]. The large difference in the decomposition temperature between $Zn(acac)_2$ ($T_{dec} \approx 248$ °C) and $Fe(acac)_3$ ($T_{dec} \approx 180$ °C) salts of almost 70 °C, obviously impedes the incorporation of zinc ions

Accepted Manuscript

into the spinel crystal structure [34, 35]. It might be also that presence of water, introduced as bounded molecules to chloride salts (in samples **2-F27** and **3- MZ17**), has negative impact on this process.

3.2 Crystal structure and microstructure analysis

Rietveld analysis. The experimental XRD patterns of all three samples, **Z18**, **F28** and **MZ17**, were fitted using *FullProf* program based on the Rietveld method. Different combinations of the isotropic/anisotropic *size* and *strain* broadening were considered during refinement of the microstructural parameters. A rather good agreement between the experimental and modeled XRD pattern was obtained when an anisotropic size broadening was considered, regardless whether the isotropic or anisotropic *strain* broadening was applied. For these two models, the obtained values for all refined parameters overlapped within the standard deviations (table S1). Further improvement in the refinement (lower goodness-of-fit, *GoF*) was achieved when, in addition to the anisotropic *size* broadening (which contribute to the Lorentzian component of the profile function), we introduced a contribution of an isotropic *size* broadening via a Gaussian function, and kept the isotropic *strain* broadening model [36]. Following this model, we observed decrease of the average apparent size (App-Size) values for about 11% (in **Z18** and **MZ17**) and 16 % (in **F28**), and the average maximum strain values for more than 50% (Max-Strain = 1/4 apparent strain Stokes-Wilson), compared to the values obtained following previous models. The comparative analysis of the refined structural and microstructural parameters for each applied model, as well as the refined and calculated cation-oxygen bond distances and the reliability factors are given for the sample **Z18** in the *Supplementary* (table S1).

Although the best agreement between the experimental and refined XRD data (the lowest *GoF*) gave the model: (*isotropic+anisotropic*) *size* and *isotropic strain* broadening, the results presented here are obtained in the frame of the model which considers an *anisotropic size* broadening and an *anisotropic strain* broadening. One of the reasons for this is that we were able to refine all parameters simultaneously, what is not quite common situation for nanocrystals (therefore, is interesting to show). The second reason is that the shape of **Z18** nanocrystallites obtained upon refinement the XRD data in this model fits in the best way the real shape of nanoparticles observed by HRTEM (figure 2(b) and 2(d)). The experimental and refined XRD data of the samples **Z18**, **F28** and **MZ17** applying a model which consider an *anisotropic size*

Accepted Manuscript

broadening and an *anisotropic strain* broadening contribution, as well as the projection on *xy*-plane of the average crystallite size and the average maximum strain in the reciprocal space, are shown in figure 3, while the main results of the Rietveld refinement are summarized in table 2.

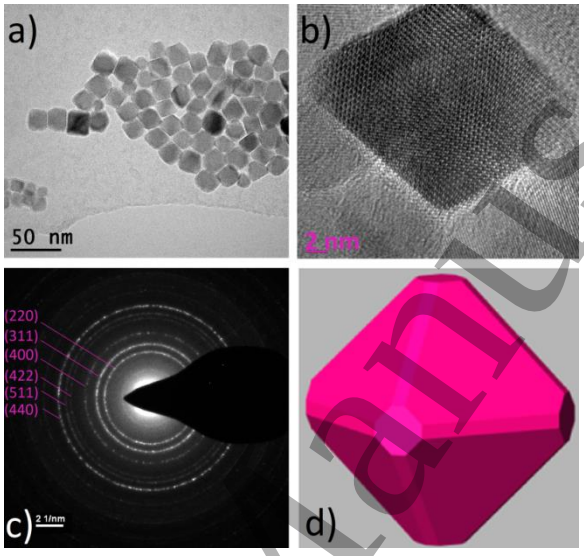

Figure 2. (a_b) HRTEM images and (c) SAED (selected area electron diffraction) pattern of the sample **Z18**; (d) shape of **Z18** nanoparticle obtained applying *anisotropic* size and *anisotropic* strain broadening model.

Accepted Manuscript

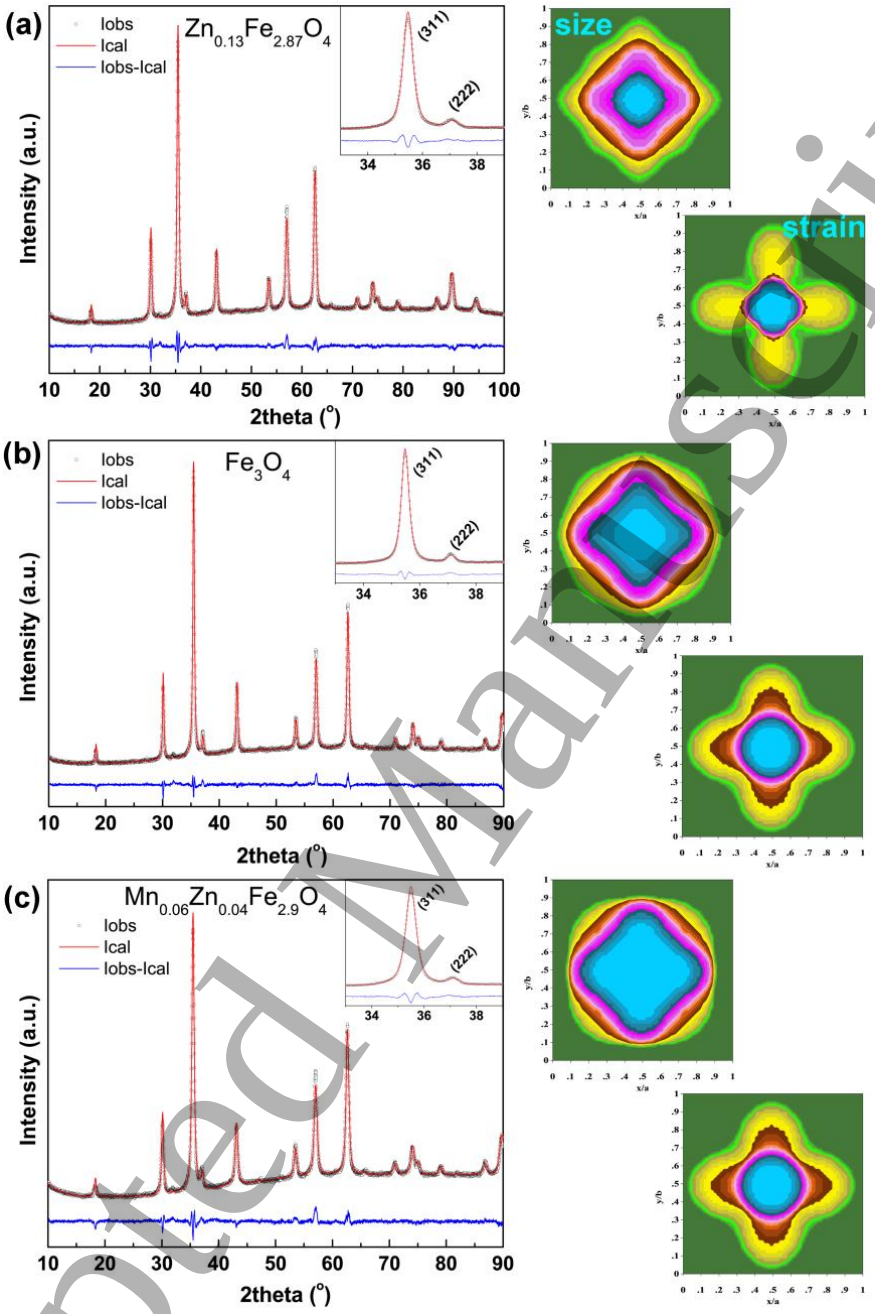

Figure 3. (left): Refined XRD patterns of the samples **Z18** (a), **F28** (b), and **MZ17** (c) in a model which consider an *anisotropic size* broadening and an *anisotropic strain* broadening contribution. (right): Visualization of the average crystallite size and the average maximum strain in the reciprocal space (projection on *xy*-plane), obtained from refinement of the patterns by *GFOURIER* program.

Accepted Manuscript

Lattice parameters show typical values of bulk magnetite and vary slightly by changing the composition, a=(8.391-8.396) Å. Slight increase of the lattice parameter, a, in Zn-doped sample, **Z18**, compared to the unsubstituted magnetite, **F28**, indicates that the Zn^{2+} ions are incorporated into the tetrahedrally coordinated, A-sites in the spinel lattice. Oppositely, slight decrease of the lattice parameter in (Mn,Zn)-containing sample, **MZ17**, compared to **F28**, could be an indication that some Mn^{2+} ions are oxidized into Mn^{3+} and sited at octahedrally coordinated, B-sites, replacing Fe^{2+} ions.

Microstructural analysis showed that the size of coherent domains, d_{XRD}, for applied model matches the average particle size estimated using TEM, $\langle d \rangle_{TEM}$ (see table 2). In addition, the shape of **Z18** nanocrystallites obtained upon refinement the XRD data fits the shape observed by HRTEM (figures 2(b) and 2(d)). A low value of the applied maximum strain (*i.e.* the microstrain) is obtained in all three samples indicating the low density of crystal imperfections. The low density of crystal imperfections is also confirmed in the sample **Z18** by HRTEM observation (figure 2(b)). In substituted Fe_3O_4 cuboctahedral nanoparticles, **Z18** and **MZ17,** with similar particle size and substitution level, x (x=0.13 and x=0.10, respectively), microstrain is almost of the same order, while in the unsubstituted magnetite **F28**, microstrain decreases (table 2). Presumably, the density of crystal imperfections in nanocrystals synthesized by thermal decomposition method can be inversely related with a particle size and/or substitution level.

Table 2. The results of Rietveld refinement of XRPD patterns of samples **1-Z18**, **2-F28** and **3-MZ17** in the model which consider a combination of an *anisotropic size* broadening and an *anisotropic* strain broadening.

Sample	**1-Z18**	**2-F28**	**3-MZ17**
Composition	$\mathbf{Zn_{0.13}Fe_{2.87}O_4}$	$\mathbf{Fe_3O_4}$	$\mathbf{Mn_{0.06}Zn_{0.04}Fe_{2.9}O_4}$
Occupancy set up at:	$(Zn^{2+}_{0.13}Fe^{3+}_{0.87})$ $[Fe^{2+}_{0.87}Fe^{3+}_{1.13}]O_4$	(Fe^{3+}) $[Fe^{2+}Fe^{3+}]O_4$	$(Mn^{2+}_{0.03}Zn^{2+}_{0.04}Fe^{3+}_{0.93})$ $[Fe^{2+}Fe^{3+}_{0.97}Mn^{3+}_{0.03}]O_4$
Average particle size, $\langle d \rangle_{TEM}$ (nm)	18.3±4.0	28±10	17.2±4.8
Average App-Size, d_{XRD}(nm)	19.7(2.0)[#]	25.9(1.6)[#]	16.1(1.1)[#]
along [111]	17.7	23.6	14.2
along [110]	20.7	28.0	17.5
along [100]	24.7	27.6	17.0
Applied Max-Strain($\times 10^{-4}$)	21(8)	13(2)	21(8)
Density, ρ (g/cm^3)	5.224	5.202	5.212

Accepted Manuscript

Lattice constant, *a* (Å)	8.3965(1)	8.3934(2)	8.3917(1)
Oxygen parameter, *u*	0.2528(2)	0.2518(2)	0.2532(2)

measure of anisotropy, no standard deviation

3.3. Mössbauer spectra analysis

To observe changes in the local environment of Fe ions caused by substituting Fe^{3+} ions with Zn^{2+} or (Zn^{2+}/$Mn^{2+/3+}$) in the spinel lattice, we used the Mössbauer spectroscopy. The experimental and fitted zero-field transmission Mössbauer spectra of **Z18**, **F28** and **MZ17** samples, collected at ambient conditions, are shown in figure 4. All three spectra are composed of two magnetic components typical for magnetite, representing two inequivalent A (tetrahedral) and B (octahedral) Fe ion positions in the spinel AB_2O_4 structure [37]. No characteristic paramagnetic components appear despite the nanoparticulate nature of the samples indicating that all particles are blocked at room temperature ($T_B^{Möss}$ > RT) for the experimental time window of measurements defined by the Mössbauer spectroscopy ($\tau_{meas}^{Möss} = \tau_{Larmor} \approx 10^{-8}$–$10^{-9}$ s for ^{57}Fe). The RT spectra of samples **F28, Z18** and **MZ17** were fitted with two, three and four magnetic sextets, respectively, giving the best results. The fitted hyperfine parameters values are summarized in table 3.

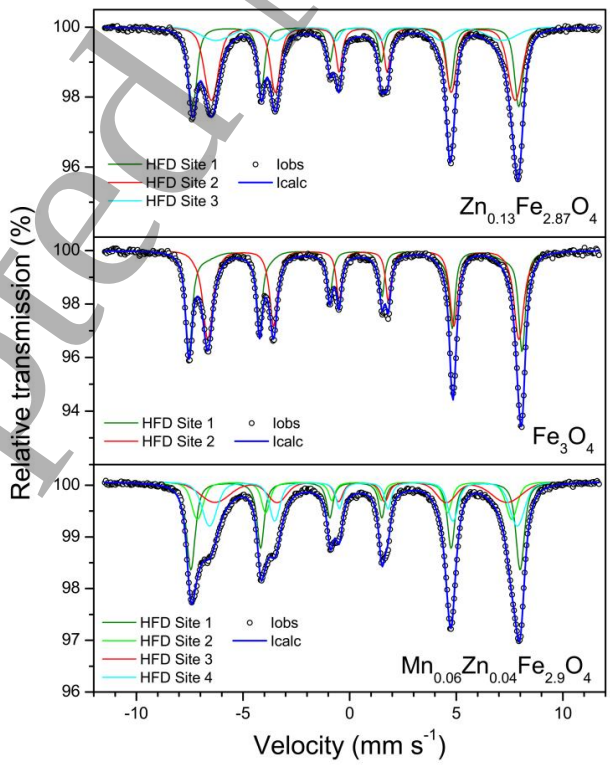

Accepted Manuscript

Figure 4. The room temperature Mössbauer spectra of sample **Z18**, **F28** and **MZ17**. In substituted samples, **Z18** and **MZ17,** the background was adjusted with an addition of a broad singlet line (with zero quadrupole splitting).

Table 3. Fitted room temperature Mössbauer parameters: δ - isomer shift, B_{hf} - magnetic hyperfine field, ε - quadrupole shift and Γ_{exp}- line width, for **Z18**, **F28** and **MZ17** samples.

Sample	**assignment**	δ (mm s^{-1})	B_{hf} (T)	ε (mm s^{-1})	*Ratio* (%)
F28	A_1: $(Fe^{3+})^{tet}$	0.29	47.7	-0.008	45.6
	B_1: $(Fe^{2+}/Fe^{3+})^{oct}$	0.65	45.3	-0.008	48.9
Z18	A_1: $(Fe^{3+})^{tet}$	0.29	47.2	-0.006	36.3
	B_1: $(Fe^{2+}/Fe^{3+})^{oct}$	0.65	44.1	-0.007	44.3
	B_2: $(Fe^{2+}/Fe^{3+})^{oct}$	0.49	41.3	0.054	15.5
MZ17	A_1: $(Fe^{3+})^{tet}$	0.28	47.9	-0.007	31.4
	A_2: $(Fe^{3+})^{tet}$	0.28	45.7	-0.050	16.51
	B_1: $(Fe^{2+}/Fe^{3+})^{oct}$	0.65	44.7	-0.009	24.27
	B_2: $(Fe^{2+}/Fe^{3+})^{oct}$	0.55	42.5	-0.020	20.80

Mössbauer spectrum of unsubstituted Fe_3O_4 (F28). Mössbauer spectrum of the sample **F28**, which is by EDX measurements identified as unsubstituted magnetite, was fitted with two magnetic components belonging to Fe ions on sites with different local surrounding. The magnetic sextet A_1 with lower isomer shift, ŭ and a higher hyperfine field, B_{hf} was attributed to the Fe^{3+} ions residing on the A sites. The second component, B_1 was assigned to the mixture of Fe^{3+} and Fe^{2+} ions at the B sites. The quadrupole shift, ε was find to be close to zero for both sites indicating symmetric charge distribution around iron nucleus. The values of the fit parameters are in good agreement with values reported in the literature for pure magnetite (even though the hyperfine fields are somewhat lower than the ones obtained for bulk magnetite) [38, 39]. However, the obtained ratio of spectral areas of A and B sextets, of $R_{A/B}$=0.97, for **F28** sample is significantly higher than the theoretical value 0.5 predicted for stoichiometric magnetite (this value is valid if the same recoil fraction is assumed for both A and B sites, and it can be slightly larger if the recoil fraction is assumed to be larger for A sites [37]). The literature results revealed that for Fe_3O_4, $R_{A/B}$=1.09±0.04 at room temperature [40]. Accordingly, we could expect a possible nonstoichiometry of the sample (the intensity of B line relative to the A line

Accepted Manuscript

reduces in nonstoichiometric magnetite [41]). This points out to the presence of larger amount of Fe^{3+} ions in the sample, indicating that the sample contains a certain amount of maghemitized magnetite [23, 42]. The broadening of the inner sextet compared to the outer one additionally indicates that our sample can be consisted of partially oxidized magnetite. Since the oxidation of magnetite is followed by the vacancy formation, the nonstoichiometric magnetite can be represented in the following form: $(Fe^{3+})_A[(Fe^{2+}Fe^{3+})_{2-6x}(Fe^{3+})_{5-x}(\square)_x]_BO_4$, where $\square$ stand for a vacancy (it is assumed that vacancy are formed exclusively on the octahedral sites of the spinel structure) [43]. Following procedure from the paper of *Costa et al* [43] we were able to estimate the amount of vacancies in the sample. It was found that the chemical formula of the sample **F28** can be $Fe_{2.92}O_4$. The estimated number of vacancies are in concordance with the previous Mössbauer studies on nonstoichiometric partially oxidized magnetite [43, 44]. However it should be noted that the lattice parameter evaluated from the XRD analysis and the observed Verwey transition temperature at ~117 K (see figure 5(a)) correspond to the magnetite with less number of vacancies [45]. Therefore we conclude that our sample **F28** probably comprises particles whose outer shell layer consists of oxidized Fe^{2+} ions while the nucleus consists of pure magnetite [46, 47].

Mössbauer spectrum of Zn-substituted Fe_3O_4 (Z18). It can be readily seen that, compared to unsubstituted Fe_3O_4, **F28**, the spectrum of Zn-doped Fe_3O_4, **Z18**, displays less resolved sextets which is the result of incorporation of the nonmagnetic Zn^{2+} ions at A sites of the magnetite spinel structure. It was reported that for low values of Zn doping ($x<0.4$ [18] or $x<1/3$ [48]), the Zn ions preferentially occupy A sites which leads to broadening of the B absorption lines. Namely, incorporation of nonmagnetic Zn^{2+} ion at the A sites cause the break of four magnetic A-B connections [22], thus leading to the weakening of A-O-B superexchange interactions and, consequently to the lowering of hyperfine fields values. Random distribution of Zn ions on A sites produces non-uniform hyperfine fields on B-sites, thus causing the line broadening of inner sextets. Therefore, the Mössbauer spectrum of Zn-substituted magnetite (figure 4), with composition $Zn_{0.13}Fe_{2.87}O_4$ predicted by EDX analysis, was fitted with three sextets. The sextet A_1 was assigned to the Fe^{3+} ions at A sites, while the two sextets, B_1 and B_2, with higher values of the isomer shift, ŭ and lower hyperfine field values, B_{hf} were attributed to the $Fe^{2+/3+}$ ions residing on B sites (see table 3). Due to the decreased magnetic coupling strength between Fe^{3+} in A and B sites (invoked by non-magnetic substitution on A-sites), hyperfine

Accepted Manuscript

fields values are slightly lower for the sample **Z18** compared to the sample **F28**. A smaller B_{hf} value of component B_2 can be associated with a part of iron ions on B sites which are coupled with lower number of Fe^{3+} ions on A-sites. In addition, the lower isomer shift value of the components assigned to the octahedral B-sites, $\check{u}_B$ (isomer shift of A sites remains almost unchanged) is due to the increased number of Fe^{3+} ions on the B sites. This excess of Fe^{3+} ions appears as a consequence of the fact that the neutral charge balance requires one Fe^{2+} ion on B site to be oxidized to Fe^{3+}, for each Fe^{3+} on A site replaced by Zn^{2+} ion, or some vacancies to be generated at B sites [48]. The relative spectral area between A and B components is significantly reduced ($R_{A/B}$=0.61) in **Z18**, due to Fe^{3+} ions replacement. Here is worth to remember that for low density of vacancies and low degree of iron substitution, the rapid electron hopping process between Fe^{2+} and Fe^{3+} ions on B-sites will not be suppressed at room temperatrure [49].

Mössbauer spectrum of (Mn,Zn)-substituted Fe_3O_4 (MF17). The Mössbauer spectrum of the Zn and Mn ions substituted Fe_3O_4 sample, **MF17,** having stoichiometry $Mn_{0.06}Zn_{0.04}Fe_{2.9}O_4$, is drastically altered compared to the other two samples. For thus low doping, Zn^{2+} ions enter only A sites replacing Fe^{3+} ions, while the XRD analysis indicates that Mn ions probably replace Fe ions on both A- and B-sites. Nevertheless, even a small amount of Mn-substituted sample strongly affects the shape and the intensity of the spectrum [50, 51]. Replacement of iron by manganese ions is evidenced by the high broadening and decreased intensity of both, and especially inner band associated with octahedral (B) sites. A more pronounced decrease of the B component intensity can be an indication that manganese ions occupies B-sites [50]. The best fit of the Mössbauer spectrum was obtained when it was fitted with four components (two for tetrahedral and two for octahedral Fe sites). Two sextets, A_1 and A_2, having the same value of isomer shifts ($\check{u}$=0.28 mm/s), but different values of hyperfine fields, are assigned to the Fe^{3+} ions on the A-sites with nonequivalent environments. Accordingly, part of the Fe^{3+} ions (A_2) are subjected to hyperfine field with lower B_{hf} values, but larger qudrupole shift, ε, implying slight distortion of charge symmetry around Fe^{3+} ions on the tetrahedral sites. It is probably due to the presence of manganese ions on B sites which introduce the Jahn-Teller distortion of crystal field symmetry [41, 51, 52]. Based on this result, in the final refinement of the XRD data of sample **MZ17**, the cation occupancy was set up so that some Mn ions occypy the B sites. Another set of two magnetic components, B_1 and B_2, with larger isomer shifts, $\check{u}$ and smaller hyperfine fields, B_{hf} (table 3), were assigned to the Fe^{2+} and Fe^{3+} ions on the

Accepted Manuscript

B-sites. The component B_2 originates from parts of the lattice where iron ions have larger number of non-magnetic ions as neighbors on A sites (therefore reduced hyperfine field), and where larger number of iron ions are oxidized to Fe^{3+} (therefore smaller isomer shift) [37, 53]. The other component, B_1, having hyperfine parameters similar to those of pure magnetite sample, can be again ascribed to the Fe^{2+}/Fe^{3+} ions on octahedral sites with electron hopping occurring in a "regular" environment, *i.e.* not having zinc and manganese ions as neighbors. Somewhat reduced hyperfine field values of the components assigned to the B sites is in concordance with previous findings on Mn doping decreasing the hyperfine fields for these sites [54].

In conclusion, the isomer shift values for A_1, A_2 and B_1 components (δ_{tet} and $\delta_{oct}(B_1)$) were found to be almost the same in all three samples, indicating that the ^{57}Fe ions on the tetrahedral (A) and partially on the octahedral (B_1) sites of spinel lattice see no changes in the electron density with the variation in particle size and the composition. Upon substitution with Zn or (Mn,Zn) ions, broadening of the magnetic sextets was observed, inferring the introduction of additional component(s) (one for Zn- and two for (Mn,Zn)-substituted sample). The additional component, delineated to the ^{57}Fe ions on octahedral B_2 sites, has the lower δ_{oct} value and weaken hyperfine magnetic fields, and can be explained as being due to the distortion in the B-sites invoked by non-magnetic substitution in the A-sublattice. At the same time, the partial oxidation of Fe^{2+} ions at B-sites takes place. The second component A_2 introduced to delineate the Mössbauer spectrum of sample **MZ17** was assigned to the ^{57}Fe ions on tetrahedral A-sites which feel distortion invoked by substitution on the B-sites, probably with manganese ions. Manganese ions has high ability to change valence state, and as Mn^{3+} it has high preference for B-sites, where can introduce additional increases of the linewidth of B components by invoking Jahn-Teller distortion [41, 52]). It is worth noting that no additional components which could be associated to α-Fe_2O_3, γ-Fe_2O_3 or FeO phase, were observed in the Mössbauer spectra in all three samples: nano-α-Fe_2O_3 has higher $B_{hf}\approx51.5$ T at RT [55]; γ-Fe_2O_3 has very symmetric Mössbauer spectra at RT [50, 56, 57]; while FeO phase should give the nonmagnetic contribution to the Mössbauer spectra since its Néel temperature is $T_N\approx200$ K [31].

3.4 Magnetic characterization.

Accepted Manuscript

Magnetic responses of unsubstituted, Zn- and (Mn,Zn)-substituted Fe_3O_4 powdered nanoparticles in a static (DC) magnetic field were studied from measurements of the field and temperature dependence of DC magnetization, M(H) and M(T). To calculate mass magnetization of samples, we performed TGA/DTA analysis. The weight loss due to evaporation of organic phase, gave the residue corresponding to 94.7, 96.5 and 92.2 wt.% of the original weight of samples **Z18**, **F28** and **MZ17**, respectively (see figure S5). Thus obtained weight loss was re-calculated taking into account that during TGA/DTA experiment the partial oxidation takes place bringing in a mixture of hematite and magnetite phases (proved by the XRD analysis).

The zero-field-cooled magnetization curves (M_{ZFC}, figure 5(a)) do not rich the maximum in a field of 7.96 kA/m (100 Oe) up to 300 K, suggesting the existence of strong interparticle interactions. The magnetic dipole-dipole interactions modify the energy barrier ϕE_A ($=K_{eff}V$; K_{eff} is an effective anisotropy constant), and shift the average blocking temperature, $<T_B>$, to higher temperature range [14]. The drop of M_{ZFC} value observed in the sample **F28** at $T_V \approx 117$ K is assigned to the Verwey transition, which should involves slight distortion of the crystal structure and change in the symmetry of crystal lattice from face centered cubic (*f.c.c*) to rhombohedral [58]. Consequently, it should bring about the transformation of the magnetocrystalline anisotropy symmetry from *cubic* to *uniaxial* when passing from $T>T_V$ to $T<T_V$ [42]. Since, in high-purity magnetite, the Verwey temperature T_V range between 110 and 125 K [59], we can assume that the core of **F28** nanoparticles has stoichiometry very close to pure Fe_3O_4 [41]. On the contrary, in doped **Z18** and **MZ17** nanoparticles, the Verwey transition has not been experimentally observed owing to the stoichiometry deviations in samples caused by the presence of chemical dopants [60, 61]. A sudden slope change in the ZFC magnetization curve, which occurs at $T_S \sim 40$ K in all three samples (figure 5(a)), could come from the relaxation processes occurring in particles with smaller size or the freezing associated with the frustrated interactions among surface spins [23, 62].

The hysteresis loops of all three samples, recorded at 300 and 5 K, are shown in figure 5 b_c. The M_S, H_C and M_R values are extracted and given in the table 4. At 5 K, the samples show a ferromagnetic behavior, with the H_C value similar in the substituted samples **Z18** and **MZ17**, and somewhat higher coercivity, H_C, in the pure **F28** magnetite. At 300 K, only unsubstituted 28 nm-sized Fe_3O_4 nanoparticles show the remanence and coecivity, while in the samples, **Z18** and **MZ17**, H_C and M_R are zero at 300 K. It means that the ensemble of 28 nm-sized unsubstituted

Accepted Manuscript

Fe_3O_4 nanoparticles exhibit weak ferrimagnetic features at 300 K coming from the part of nanoparticles which size exceeds the critical value for superparamagnetic behavior and, therefore, the thermal energy is not enough to overcome the energy barrier, ϕE_A. The saturation magnetization values, M_S at 5 K range from 91.2 Am^2/kg (sample **MZ17**) to 98.6 Am^2/kg_{Fe3O4} (sample **Z18**), overcoming the M_S value of bulk magnetite (~95 Am^2/kg) in Zn-substituted sample (table 4). With increasing temperature up to 300 K, M_S value remains high in **Z18** and **F28** (see table 4), indicating the good crystalinity and low density of the structural defects in magnetite particles with size below 30 nm [63]. The maghemitized surface layer, predicted by Mössbauer spectra analysis in **F28**, as well as the surface spin disorder, have a minor (decreasing) effect on the M_S value.

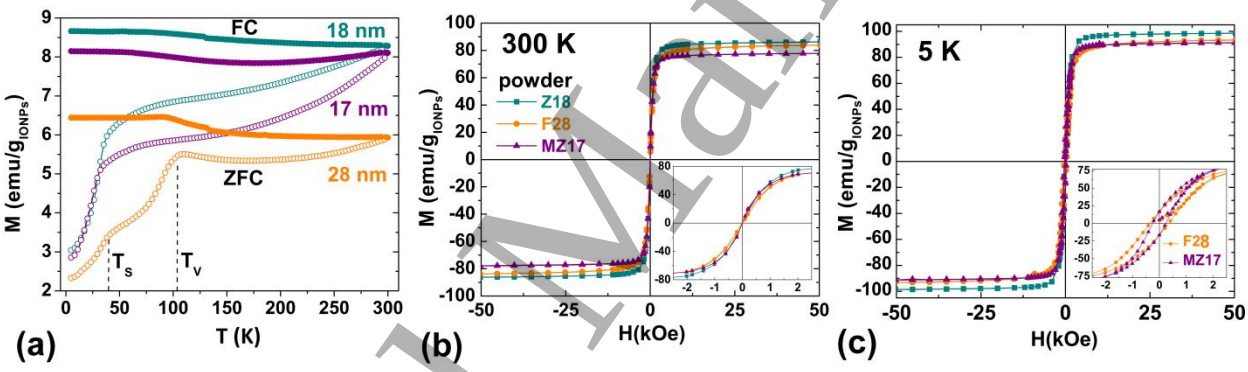

Figure 5. (a) ZFC and FC magnetizations as a function of temperature, measured with an external applied field of 7.96 kA/m (100 Oe); (b_c) the hysteresis loops of unsubstituted (**F28**), and Zn- (**Z18**) and (Mn,Zn)-substituted (**MZ17**) magnetite nanoparticles recorded at 300 K (b) and 5 K (c).

Table 4. Saturation magnetization ($\boldsymbol{M_S}$), coercitive field ($\boldsymbol{H_C}$), ratio $\boldsymbol{M_R/M_S}$ and the magnetic moment per formula unit ($\boldsymbol{\mu_{eff}}$), estimated from the hysteresis loops measured at 300 and 5 K; an effective anisotropy constant ($\boldsymbol{K_{eff}}$) at 5 K estimated from slow, DC magnetic measurements; the heating efficiency of ferrofluids expressed by the specific absorption rate (***SAR***), measured in the AC magnetic field (H_0=23.87 kA/m and f=228 kHz (for **Z18** and **F28**) or 252 kHz (for **MZ17**)); the intrinsic loss parameter (***ILP***).

Accepted Manuscript

Sample	300 K			5 K						
	M_S [Am^2/kg]	H_C [kA/m]	μ_{eff} [ε_B]	M_S [Am^2/kg]	M_R/M_S	H_C [kA/m]	μ_{eff} [ε_B]	K_{eff} [kJ/m^3]	*SAR* [W/g_{Fe}]	*ILP* [nHm^2/kg]
1-**Z18**	86.2	~0	3.6	98.6	0.17	19.1	4.1	12.9	525	4.04
2-**F28**	83.6	2.23	3.5	93.3	0.18	27.45	3.9	17.4	285	2.19
3-**MZ17**	77.6	~0	3.2	91.2	0.18	19.5	3.8	12.1	426	2.97

In order to estimate the effective magnetic anisotropy constant K_{eff}, we have used a simple analytical approach based on the relation between the coercivity of magnetic nanoparticles, H_C, and the magnetic anisotropy energy of single domain nanoparticles, φE_A, with *uniaxial* symmetry, represented by the equation: $\mu_0 H_C = 0.48\ (2K_{eff}/M_S)\ [1-(T/T_B)^{\gamma}]$ [33, 64]. The fact that K_{eff} of the ensemble of magnetic nanoparticles depends on the distribution of the easy axes of magnetization in space is partially delineated with the parameter γ, which takes value 0.77 for an ensemble of randomly oriented particles and 0.5 for an ensemble of aligned particles [65]. In our case the term (T/T_B) can be neglected, since the ZFC-FC magnetization measurements point out that the blocking temperature of samples is high. Thus, using the simplified formula, $K_{eff}=\varepsilon_0 H_C M_S/0.96$, the experimental H_C and M_S values obtained from the hysteresis loops at 5 K (table 4), as well as the density of material, ρ given as the output of XRD refinements, we estimated K_{eff} values of 12.9, 17.4 and 12.1 kJ/m^3 for **Z18**, **F28** and **MZ17**, respectively. These values are rather consistent with those found in the literature [66]. Just to note that the K_{eff} value will be increased for approximately 6% in **Z18** and **MZ17**, *e.g.* ~4% in **F28**, considering the *random* distribution of nanoparticles, and maximum ~15% for an assembly of *aligned* nanocrystallites (γ=0.5) (we suppose the T_B lies between 200 and 300 K in the substituted, and ~300 K in unsubstituted Fe_3O_4). Even with such increments, K_{eff} would be below 20 kJ/m^3.

Such estimated K_{eff} value (from DC magnetic measurements at $T<<T_B$) usually is related to the single-particle anisotropy properties at room temperature [67, 68]. According to it, the K_{eff} value in the substituted samples, **Z18** and **MZ17**, is very close to the first order magnetocrystalline anisotropy constant, K_1 of bulk magnetite regarding the *cubic* symmetry

Accepted Manuscript

(intermediate literature value for $K_1(Fe_3O_4)$ is between 11 and 14 kJ/m^3 [23, 42, 69]. In unsubstituted **F28** sample, the resulting anisotropy constant K_{eff} is higher than K_1 probably due to the contribution of the shape anisotropy (should be considered for elongated NPs with the aspect ratio >1.1 [67]), and/or the anisotropy coming from the magneto-dipole interaction of the particles. It is well known that with increasing particle size, the interparticle interactions increases and tend to form aggregates of nanocrystals [70]. Additionally, it seems that the surface anisotropy can be neglected in all three samples due to the diminishing effect of surface spin disordered in cubic-like nanoparticles at low temperatures [20, 70]. Following the simple analytical approach, the anisotropy properties of **Z18** and **MZ17** samples seem to be dominated by crystal-field effect [69, 71].

It is worth mentioning that the problem with estimation of K_{eff} still remain opened for nanoparticulate systems. For an ensemble of the magnetic nanoparticles it is difficult to evaluate K_{eff} due to the fact that apart from the magnetocrystalline, the shape and the surface anisotropies, the anisotropy comes from interparticle interactions and is dependent on the configuration of the particles inside ensembles (*i.e.* orientation of their easy axis of magnetization relative to the applied magnetic field). When an ensemble of magnetic nanoparticles is subject to an alternating current (AC) magnetic field (as in magnetic hyperthermia application), then the effective anisotropy K_{eff} can be changed (the magnetization process, as well as the topology of the particles can be changed). Thus, K_{eff} may obey particular dependence upon the frequency, f and AC field amplitude, H_0 variations [70, 72, 73]. This fact can significantly change the hyperthermia efficiency of magnetic nanoparticles. Comparing some literature results based on ferromagnetic resonance experiments, we may expect decrease of the K_{eff} with increasing frequency f [70], as well as with a field amplitude H_0 increase [72]. Additionally, a significant reduce of the K_{eff} can be found in *in vivo* conditions, when IONPs are taken by live cells [14]. With decreasing the K_{eff} value, a metastable regime of heating can be established in AC magnetic fields.

More realistic description of the K_{eff} can be obtained from the numerical calculations for multi-particle systems. Another alternative approach is an atomistic spin model [74]. These methods should involve the consideration of the surface spin disorder, the shape anisotropy, the topology of the nanoparticles in an ensemble, the diamagnetic contribution, the Zeeman's

Accepted Manuscript

splitting of atomic energy levels in the magnetic field. A complexity of determining the K_{eff} values (especially under AC magnetic conditions) are reflected on a heating efficiency study.

3.5 Heating abilities of pure, Zn- and (Mn,Zn)-doped samples.

In figure 6 are shown the heating ability of oleic acid (OA)-coated magnetic **Z18**, **F28** and **MZ17** nanoseeds dispersed in hexane, when the nanoparticle were exposed to AC magnetic field of amplitudes, H_0 in the range between 7 and 23.87 kA/m and frequency f=228 or 252 kHz. Some characteristic hyperthermia curves of the samples are given in figure S6. The values of the intensity of magnetic field H_0 and frequency f are in the range commonly used in the literature [6, 20, 21, 65], even though their product, $H_0 \times f$ (between 1.6×10^9 and 6.0×10^9 $Am^{-1}s^{-1}$), exceeds the value limited by the Atkinson-Brezovich criterion (4.85×10^8 $Am^{-1}s^{-1}$) [75], for one order of magnitude. If we assume that the magnetic hyperthermia treatment will be applied locally (for tissue heating), the use of larger field-frequency product may be considered tolerable for the human body [76].

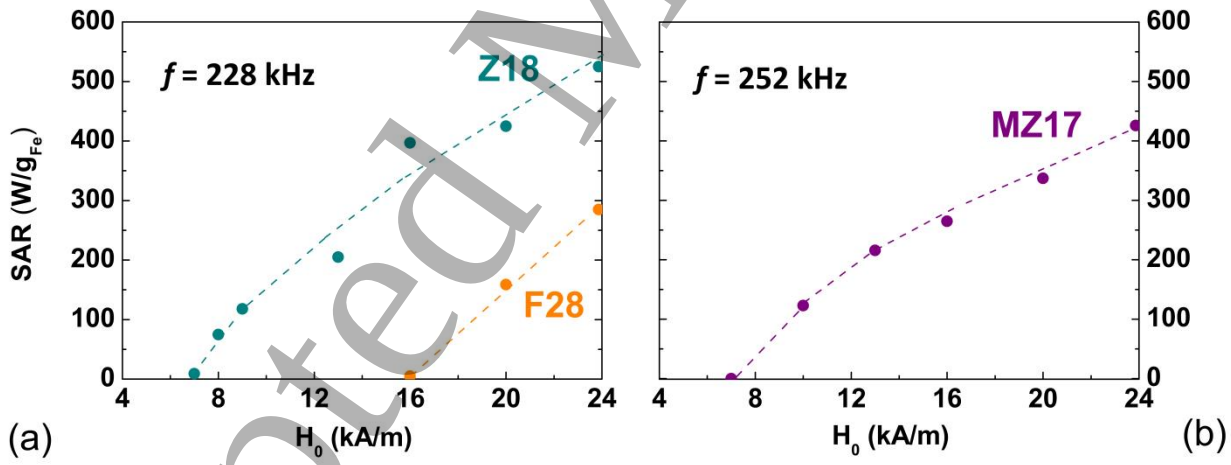

Figure 6. The *SAR* values of samples (a) **Z18** and **F28** and (b) **MZ17** measured at frequency f, for different applied magnetic fields. Dash-line is a guide for eyes.

As we can see from figure 6, the increase of *SAR* value upon field amplitude is observed for higher H_0 values in all three samples, with the difference in the offset of the heating for substituted and unsubstituted samples. Substituted samples, **Z18** and **MZ17**, start to release heat

Accepted Manuscript

before the **F28** ferrofluid (*i.e.* **F28** nanoseeds needs higher amplitude of the applied field, H_0, to start to generate heat). The estimated *SAR* values of three samples seems to be correlated with the field cooled (FC) magnetization value, M_{FC}, measured in a low field of 7.96 kA/m (100 Oe), as well as the saturation magnetization to coercivity ratio, M_S/H_C, at 5 K. The unsubstituted magnetite nanoparticles, **F28**, have the lowest M_{FC} and M_S/H_C values and consequently lower heating potential under the same experimental conditions (H_0,f), in comparison with **Z18** and **MZ17**. This can be partially due to the broader particle size distribution in **F28** (bigger NPs, which stay blocked and do not participate in the transformation of magnetic to thermal energy), as well as to the formation of nanoclusters. The relaxation time for nanoclusters and single nanoparaticles can differ [77], consequently bringing the changes in the heating abilities (*i.e.* *SAR* values). In addition, the lower intrinsic loss parameters value, *ILP* ($ILP = SAR/(H_0^2 f)$), could also indicate on the formation of nanoclusters in the sample **F28** (see table 4). Zinc-substituted Fe_3O_4 cubo-octahedrons, **Z18**, show the best heating performances. This sample has a good potential for using in the hyperthermia therapy. On inspection of literature, we just mention some *SAR* and *ILP* values of nanoparticles similar in size, composition and shape with here studied ones. Thus, 18nm-sized $Zn_{0.4}Fe_{2.6}O_4$ cubes have shown *SAR*=1860 W/g at H_0 = 37.4 kA/m and f = 500 kHz (*ILP* = 2.66 nH m^2/kg) [20], while 15.4nm-sized $Zn_{0.4}Fe_{2.6}O_4$ cubes possess higher heating potential, *i.e.* *SAR*=1019.2 W/g at H_0 = 16 kA/m and f = 380 kHz, and *ILP* = 10.5 nH m^2/kg [6]. On the other hand, 17nm- and 26nm-sized octopods of composition FeO-Fe_3O_4 have *SAR* and *ILP* values of ~190 and 150 W/g and 1 and 0.8 nH m^2/kg, respectively, when are exposed to AC field of H_0 = 24.67 kA/m and f = 310 kHz [65]. Bigger iron oxide nanocubes, with an average size ~23 nm have *SAR*=375 W/g$_{Fe}$ at H_0 = 24 kA/m and f = 301 kHz [21], and very similar *ILP* value (2.16 nH m^2/kg), as our **F28** nanoparticles. To what extent the heating ability of our nanoparticles will be influenced by the media viscosity, clustering and interparticle interactions will be a task for our future investigations.

Conclusion

The single crystalline Fe_3O_4-based nanoparticles, pure or substituted by zinc or (zinc, manganese) of size above 15 nm were fabricated by a thermal decomposition of metal precursors. The incorporation of Zn^{2+} ions into a spinel structure was found to be difficult, even

Accepted Manuscript

though two different sources of Zn^{2+} ions were used, $Zn(acac)_2$ and $ZnCl_2$ salt. The XRD analysis revealed presence of the pure magnetite-based phase in all three samples. In terms of crystallinity and size dispersion, this synthesis protocol shows superiority over decomposition of iron oleate and the co-precipitation synthesis route. High saturation magnetization and single magnetic phase were detected in all three samples. Slightly cation-deficient magnetite phase could only be presented at the nanoparticle's surface, but is negligible for magnetization diminution. 18nm-sized $Zn_{0.13}Fe_{2.87}O_4$ cuboctahedrons, with the specific absorption rate, $SAR \cong$ 425 W/g_{Fe} at H_0=20 kA/m and f=228 kHz, show the best heating performance.

Acknowledgments

The article is based upon work from COST Action RADIOMAG (TD1402), supported by COST (European Cooperation in Science and Technology). N.J.O. gives special thanks to Prof. Gerardo F. Goya of University of Zaragoza for his support to get STSM grant and for providing work facilities at the Institute of Nanoscience of Aragón. N.J.O. and M.M.M. acknowledge the Ministry of Education, Science and Technological Development of the Serbian Republic for financial support through the projects No. 45015 and 171027. T.E.T. acknowledge financial support from the Spanish Ministerio de Economia y Competitividad (MINECO) through project MAT2016-78201-P and by the Aragón Regional Government (DGA), through the Research Groups grants (E-26 and E28-17R) co-financed by the FEDER Operational Program Aragón 2014ï 2020 ñBuilding Europe from Aragonò. We are grateful to the Advanced Microscopy Laboratory (LMA) and the SAI-UZ for technical assistance. We thank Dr. V. Spasojeviĺ for the magnetometer measurements, Dr. V. Ivanoski and Dr. A. Umiĺeviĺ for the Mössbauer spectra collecting, Prof. N. Cvjetiĺanin for TGA/DTA data collecting and Prof. A. Kremenoviĺ for critical reading of the text.

REFERENCES

[1] Xu C and Sun S 2013 New forms of superparamagnetic nanoparticles for biomedical applications *Adv. Drug Delivery Rev.* **65** 732-43

[2] Torres-Lugo M and Rinaldi C 2013 Thermal potentiation of chemotherapy by magnetic nanoparticles *Nanomedicine* **8(10)** 1689ï 1707

Accepted Manuscript

[3] Zhu Y -F, Ni Q -Q, Fu Y -Q and Natsuki T 2013 Synthesis and microwave absorption properties of electromagnetic functionalized Fe_3O_4ï polyaniline hollow sphere nanocomposites produced by electrostatic self-assembly *J. Nanopart. Res.* **15** 1988

[4] Zhang J and Yu A 2015 Nanostructured transition metal oxides as advanced anodes for lithium-ion batteries *Sci. Bull.* **60(9)** 823ï 38

[5] Jang J -t, Nah H, Lee J -H, Moon S H, Kim M G and Cheon J 2009 Critical Enhancements of MRI Contrast and Hyperthermic Effects by Dopant-Controlled Magnetic Nanoparticles *Angew. Chem. Inter. Ed.* **48** 1234-38

[6] Bauer L M, Situ S F, Griswold M A and Samia A C S 2016 High-performance iron oxide nanoparticles for magnetic particle imaging ï guided hyperthermia (hMPI) *Nanoscale* **8** 12162

[7] Goya G F, Grazu V and Ibarra M R 2008 Magnetic Nanoparticles for Cancer Therapy *Curr. Nanosci.* **4** 1-16

[8] Starsich F H L, Eberhardt C, Boss A, Hirt A M and Pratsinis S E 2018 Coercivity Determines Magnetic Particle Heating *Adv. Helathcare Mater*. 1800287

[9] Tong S, Quinto C A, Zhang L, Mohindra P and Bao G 2017 Size-Dependent Heating of Magnetic Iron Oxide Nanoparticles *ACS Nano* **11** 6808-16

[10] Iacovita C, Florea A, Dudric R, Pall E, Iulian Moldovan A, Tetean R, Stiufiuc R and Lucaciu C M 2016 Small versus Large Iron Oxide Magnetic Nanoparticles: Hyperthermia and Cell Uptake Properties *Molecules* **21** 1357

[11] Xie W, Guo Z, Gao F, Gao Q, Wang D, Liaw B-s, Cai Q, Sun X, Wang X and Zhao L 2018 Shape-, size- and structure-controlled synthesis and biocompatibility of iron oxide nanoparticles for magnetic theranostics *Theranostic* **8** 3284-307

[12] Noh S -H, Ho Moon S, Shin T-H, Lim Y and Cheon J 2017 Recent advances of magneto-thermal capabilities of nanoparticles: From design principles to biomedical applications *Nano Today* **13** 61-76

[13] Hao R, Xing R, Xu Z, Hou Y, Gao S and Sun S 2010 Synthesis, Functionalization, and Biomedical Applications of Multifunctional Magnetic Nanoparticles *Adv. Mater.* **22** 2729ï 42

[14] Cabrera D, Coene A, Leliaert J, Artés-Ibáñez E J, Dupré L, Telling N D and Teran F J 2018 Dynamical Magnetic Response of Iron Oxide Nanoparticles Inside Live Cells *ACS Nano* **12** 2741-52

Accepted Manuscript

[15] Das R, Alonso J, Nemati Porshokouh Z, Kalappattil V, Torres D, Phan M -H, Garaio E, Ángel García J, Sanchez Llamazares J Land Srikanth H 2016 Tunable High Aspect Ratio Iron Oxide Nanorods for Enhanced Hyperthermia *J. Phys. Chem*. C **120** 10086-93

[16] Moya C, Batlle X and Labarta A 2015 The effect of oleic acid on the synthesis of $Fe_{3-x}O_4$ nanoparticles over a wide size range *Phys. Chem. Chem. Phys*. **17** 27373-79

[17] Bárcena C, Sra A K, Chaubey G S, Khemtong C, Ping Liu J and Gao J 2008 Zinc ferrite nanoparticles as MRI contrast agents *Chem. Comm*. 2224-26

[18] Yang Y, Liu X, Yang Y, Xiao W, Li Z, Xue D, Li F and Ding J 2013 Synthesis of nonstoichiometric zinc ferrite nanoparticles with extraordinary room temperature magnetism and their diverse applications *J. Mater. Chem. C* **1** 2875-85

[19] Kolhatkar A G, Chen Y -T, Chinwangso P, Nekrashevich I, Dannangoda G C, Singh A, Jamison A C, Zenasni O, Rusakova I A, Martirosyan K S, Litvinov D, Xu S, Willson R C and Randall Lee T 2017 Magnetic Sensing Potential of Fe_3O_4 Nanocubes Exceeds That of Fe_3O_4 Nanospheres *ACS Omega* **2** 8010-19

[20] Noh S -H, Na W, Jang J -t, Lee J -H, Jung Lee E, Ho Moon S, Lim Y, Shin J -S and Cheon J 2012 Nanoscale Magnetism Control via Surface and Exchange Anisotropy for Optimized Ferrimagnetic Hysteresis *Nano Lett*. **12** 3716-21

[21] Lak A, Cassani M, Mai B T, Winckelmans N, Cabrera D, Sadrollahi E, Marras S, Remmer H, Fiorito S, Cremades-Jimeno L, Jochen Litterst F, Ludwig F, Manna L, Teran F J, Bals S and Pellegrino T 2018 Fe^{2+} Deficiencies, FeO Subdomains, and Structural Defects Favor Magnetic Hyperthermia Performance of Iron Oxide Nanocubes into Intracellular Environment *Nano Lett.* **18** 6856ï 66

[22] Mendoza Zélis P, Pasquevich G A, Stewart S J, Fernández van Raap M B, Aphesteguy J, Bruvera I J, Laborde C, Pianciola B, Jacobo S, Sánchez F H, Structural and magnetic study of zinc-doped magnetite nanoparticles and ferrofluids for hyperthermia applications 2013 *J. Phys. D: Appl. Phys*. **46** 125006

[23] Andrés Vergés M, Costo R, Roca A G, Marco J F, Goza G F, Serna C J and Morales M P 2008 Uniform and water stable magnetite nanoparticles with diameters around the monodomainï multidomain limit *J. Phys. D: Appl. Phys.* **41** 134003

Accepted Manuscript

[24] Pacakova B, Kubickova S, Salas G, Mantlikova A, Marciello M, Morales M P, Niznansky D and Vejpravova J 2017 Internal structure of magnetic nanoparticle determines magnetic response *Nanoscale* **9** 5129-40

[25] Ichikawa R U, Roca A G, López-Ortega A, Estrader M, Peral I, Turrillas X and Nogués J 2018 Combining X-Ray Whole Powder Pattern Modeling, Rietveld and Pair Distribution Function Analyses as a Novel Bulk Approach to Study Interfaces in Heteronanostructures: Oxidation Front in FeO/Fe_3O_4 Core/Shell Nanoparticles as a Case Study *Small* **14** e1800804

[26] Jovií Orsini N, Babií-Stojií B, Spasojevií V, Calatayud M P, Cvjetií anin N and Goya G F 2018 Magnetic and power absorption measurements on iron oxide nanoparticles synthesized by thermal decomposition of $Fe(acac)_3$ *J. Magn. Magn. Mater.* **449** 286-96

[27] Bonsdorf G, Denecke M A, Schäfer K, Christen S, Langbein H and Gunβer W 1997 X-ray absorption spectroscopic and Mössbauer studies of redox and cation-ordering processes in manganese ferrite *Solid State Ion.* **101-103** 351-57

[28] Rodríguez-Carvajal J 2001 Recent developments of the program FULLPROF *IUCr Commission on powder diffraction Newsletter* **26** 12-19

[29] Stephens P W 1999 Phenomenological model of anisotropic peak broadening in powder diffraction *J. Appl. Phys*. **32** 281-89

[30] Cheon J -W, Seo J -W and Lee J -H 2006 Preparation method of magnetic and metal oxide nanoparticles, Korean PATENT PCT WO 2006/052042 A1 (https://www.google.com/patents/WO2006052042A1)

[31] Lak A, Kraken M, Ludwig F, Kornowski A, Eberbeck D, Sievers S, Litterst F J, Weller H and Schilling M 2013 Size dependent structural and magnetic properties of FeOï Fe_3O_4 nanoparticles *Nanoscale* **5** 12286-95

[32] Shavel A, Rodríguez-González B, Pacifico J, Spasova M, Farle M and Liz-Marzán L M 2009 Shape Control in Iron Oxide Nanocrystal Synthesis, Induced by Trioctylammonium Ions *Chem. Mater*. **21** 1326-32

[33] Yang H, Ogawa T, Hasegawa D and Takahash M 2008 Synthesis and magnetic properties of monodisperse magnetite nanocubes *J. Appl. Phys*. **103** 07D526

[34] Liang W -I, Zhang X, Bustillo K, Chiu C -H, Wu W -W, Xu J, Chu Y -H and Zheng H 2015 In Situ Study of Spinel Ferrite Nanocrystal Growth Using Liquid Cell Transmission Electron Microscopy *Chem. Mater*. **27** 8146-52

Accepted Manuscript

[35] Baird N, Losovyj Y, Yuzik-Klimova E Yu, Kuchkina N V, Shifrina Z B, Pink M, Stein B D, Morgan D G, Wang T, Rubin M A, Sidorov A I, Sulman E M and Bronstein L M 2016 Zinc-Containing Magnetic Oxides Stabilized by a Polymer: One Phase or Two? *ACS Appl. Mater. Interfaces* **8** 891ï 99

[36] https://www.ill.eu/sites/fullprof/php/tutorials.html

[37] Gorski C A and Scherer M M 2010 Determination of nanoparticulate magnetite stoichiometry by Mössbauer spectroscopy, acidic dissolution, and powder X-ray diffraction: A critical review *Am. Mineral.* **95** 1017ï 26

[38] Woo K, Hong J, Choi S, Lee H -W, Ahn J -P, Kim C S and Lee S W 2004 Easy Synthesis and Magnetic Properties of Iron Oxide Nanoparticles *Chem. Mater.* **16** 2814-18

[39] Dézsi I, Fetzer Cs, GombkötĻ Á, SzĬcs I, Gubicza J and Ungár T 2008 Phase transition in nanomagnetite *J. Appl. Phys.* **103** 104312

[40] Annersten H and Hafner S S 1973 Vacancy distribution in synthetic spinels of the series Fe_3O_4 -γ-Fe_2O_3 *Z. Kristallogr.* **137** 321-40

[41] Schmidbauer E and Keller M 2006 Magnetic hysteresis properties, Mössbauer spectra and structural data of spherical 250 nm particles of solid solutions Fe3O4 ï ɔ-Fe2O_3 *J. Magn. Magn. Mater.* **297** 107-17

[42] Lima Jr E, Brandl A L, Arelaro A D and G. F. Goya 2006 Spin disorder and magnetic anisotropy in Fe_3O_4 nanoparticles *J. Appl. Phys.* **99** 083908

[43] da Costa G M, Blanco-Andujar C, De Grave E and Pankhurst Q A 2014 Magnetic nanoparticles for in vivo use: A critical assessment of their composition *J. Phys. Chem. B* **118** 11738-46

[44] Ramdani A, Steinmetz J, Gleitzer C, Coey J M D and Friedt J M 1987 Perturbation de l'echange electronique rapide par les lacunes cationiques dans $Fe_{3ī\ x}O_4$ (x⩽ 0, 09) *J. Phys. Chem. Solids* **48** 217-28

[45] Yang J B, Zhou X D, Yelon W B, James W J, Cai Q, Gopalakrishnan K V, Malik S K, Sun X C and Nikles D E 2004 Magnetic and structural studies of the Verwey transition in $Fe_{3ī\ ŭ}O_4$ nanoparticles *J. Appl. Phys.* **95** 7540-42

[46] Santoyo Salazar J, Perez L, de Abril O, Truong Phuoc L, Ihiawakrim D, Vazquez M, Greneche J M, Begin-Colin, S and Pourroy G 2011 Magnetic iron oxide nanoparticles in 10ī 40

Accepted Manuscript

nm range: composition in terms of magnetite/maghemite ratio and effect on the magnetic properties *Chem. Mater.* **23** 1379-86

[47] Daou T J, Pourroy G, Bégin-Colin S, Greneche J M, Ulhaq-Bouillet C, Legaré P, Bernhardt P, Leuvrey C and Rogez G 2006 Hydrothermal synthesis of monodisperse magnetite nanoparticles *Chem. Mater.* **18** 4399-404

[48] Wen M, Li Q and Li Y 2006 Magnetic, electronic and structural properties of $Zn_xFe_{3-x}O_4$ *J. Electron Spectros. Relat. Phenomena* **153** 65-70

[49] Handke B, Haber J, ś lńzak T, Kubik M and Korecki J 2001 Magnesium interdiffusion and surface oxidation in magnetite epitaxial films grown on MgO (100) *Vacuum* **63** 331-36

[50] Olivier L C A, Fabris J D, Rios R R V A, Mussel W N and Lago R M 2004 $Fe_{3\bar{1}\ x}Mn_xO_4$ catalysts: phase transformations and carbon monoxide oxidation *Appl. Catal.* A *Gen*. **259** 253-59

[51] Antic B, Kremenovic A, Jovic N, Pavlovic M B, Jovalekic C, Nikolic A S, Goya G F and Weidenthaler C 2012 Magnetization enhancement and cation valences in nonstoichiometric $(Mn,Fe)_{3-\tilde{u}}O_4$ nanoparticles *J. Appl. Phys* **111** 074309

[52] Lotgering F K and Van Diepen A M 1973 Valencies of manganese and iron ions in cubic ferrites as observed in paramagnetic Mössbauer spectra *J. Phys. Chem. Solids* **34** 1369-77

[53] Di Corato R, Aloisi A, Rella S, Grenèche J -M, Pugliese G, Pellegrino T, Malitesta C O and Rinaldi R 2018 Maghemite Nanoparticles with Enhanced Magnetic Properties: One Pot Preparation and Ultrastable Dextran Shell ACS *Appl. Mater. Interfaces* **10** 20271ī 80

[54] Sorescu M, Diamandescu L, Brand R A and Tarabasanu-Mihaila D 2004 Mössbauer study of manganese-doped magnetite below the Verwey transition *Mater. Lett.* **58** 885-88

[55] Greenwood N N and Gibb T C 1971 *in Mössbauer Spectroscopy* (London: Chapman and Hall Ltd) p 241

[56] Martinez B, Roig A, Obrados X, Molins E, Rouanet A and Monty C 1996 *J. Appl. Phys*. **79** 2580-86

[57] Fock J, Bogart L K, González-Alonso D, Espeso J I, Hansen M F, Varón M, Frandsen C, Pankhurst Q A *J. Phys. D: Appl. Phys*. **50** 265005

[58] Palmer W 1963 Magnetocrystalline anisotropy of magnetite at low temperature *Phys. Rev*. **131** 1057-62

Accepted Manuscript

[59] Koğodziej T, Kozğowski A, Piekarz P, TabiŜ W, KŃkol Z, ZajŃc M, Tarnawski Z, Honig J M, OleŜ A M and Parlinski K 2012 Nuclear inelastic scattering studies of lattice dynamics in magnetite with a first-and second-order Verwey transition *Phys. Rev*. B **85** 104301

[60] Aragón R, Buttrey D J, Shepherd J P and Honig J M 1985 Influence of nonstoichiometry on the Verwey transition *Phys. Rev*. B **31** 430-36

[61] Özdemir O, Dunlop D J and Moskowitz B M 1993 The effect of oxidation on the Verwey transition in magnetite *Geophys. Res. Lett.* **20** 1671-74

[62] Daou T J, Grenèche J M, Pourroy G, Buathong S, Derory A, Ulhaq-Bouillet C, Donnio B, Guillon D and Begin-Colin S 2008 Coupling Agent Effect on Magnetic Properties of Functionalized Magnetite-Based Nanoparticles *Chem. Mater.* **20** 5869ï 75

[63] Nedelkoski Z, Kepaptsoglou D, Lari L, Wen T, Booth R A, Oberdick S D, Galindo P L, Ramasse Q M, Evans R F L, Majetich S and Lazarov V K 2017 Origin of reduced magnetization and domain formation in small magnetite nanoparticles *Sci. Rep*. **7** 45997

[64] Stoner E C and Wohlfarth E P 1948 A mechanism of magnetic hysteresis in heterogeneous alloys *Phil. Trans. R. Soc*. **A240** 599ï 642

[65] Nemati Z, Alonso J, Martinez L M, Khurshid H, Garaio E, Garcia J A, Phan M H and Srikanth H 2016 Enhanced Magnetic Hyperthermia in Iron Oxide Nano-Octopods: Size and Anisotropy Effects *J. Phys. Chem*. C **120** 8370ï 79

[66] Mulea A, Muñoz D, Martín-Rodríguez R, Orue I, Garaio E, Abad Díaz de Cerio A, Alonso J, Ángel García J, Luisa Fdez-Gubieda M 2016 Optimal Parameters for Hyperthermia Treatment Using Biomineralized Magnetite Nanoparticles: Theoretical and Experimental Approach *J. Phys. Chem.* C **120** 24437-48

[67] Usov N A and Barandiaran J M 2012 Magnetic nanoparticles with combined anisotropy *J. Appl. Phys*. **112** 053915

[68] Schmitz D, Schmitz-Antoniak C, Warland A, Darbandi M, Haldar S, Bhandary S, Eriksson O, Sanyal B and Wende H 2014 The dipole moment of the spin density as a local indicator for phase transitions *Sci. Rep*. **4** 5760

[69] ř eznílek R, Chlan V, Ġtěpánková H, Novák P and Maryğko M 2012 Magnetocrystalline anisotropy of magnetite *J. Phys*.: *Condens. Matter* **24** 055501

Accepted Manuscript

[70] Charilaou M, Sahu K K, Faivre D, Fischer A, García-Rubio I and Gehring A U 2011 Evolution of magnetic anisotropy and thermal stability during nanocrystal-chain growth *Appl. Phys. Lett*. **99** 182504

[71] Kakol Z and Honig J M 1989 Influence of deviations from ideal stoichiometry on the anisotropy parameters of magnetite $Fe_{3(1\tilde{i}\ \check{u})}O_4$ *Phys. Rev.* B **40** 9090

[72] Ivanov A O, Kantorovich S S, Zverev V S, Elfimova E A, Lebedev A V and Pshenichnikov A F 2016 Temperature-dependent dynamic correlations in suspensions of magnetic nanoparticles in a broad range of concentrations: a combined experimental and theoretical study *Phys. Chem. Chem. Phys.* **18** 18342-52

[73] Usov N A 2010 Low frequency hysteresis loops of superparamagnetic nanoparticles with uniaxial anisotropy *J. Appl. Phys*. **107** 123909

[74] Moreno R, Poyser S, Meilak D, Meo A, Jenkins S, Lazarov V K, Vallejo-Fernandez G, Majetich S and Evans R F L 2019 The role of faceting and elongation on the magnetic anisotropy of magnetite Fe_3O_4 nanocrystals arXiv:1909.02470v1

[75] Atkinson W J, Brezovich I A and Chakraborty D P 1984 Usable Frequencies in Hyperthermia with Thermal Seeds *IEEE Trans. Biomed. Eng.* **31** 70ï 5

[76] Hergt R and Dutz S 2007 Magnetic particle hyperthermia-biophysical limitations of a visionary tumour therapy *J. Magn. Magn. Mater*. **311** 187ï 192

[77] Wu K and Wang J P 2017 Magnetic hyperthermia performance of magnetite nanoparticle assemblies under different driving fields *AIP Advances* **7** 056327

Accepted Manuscript